Numerical analysis of thermal fluid transport behavior during electron beam welding of 2219 aluminum alloy plate

Cheng-cai LIU, Jing-shan HE

State key Laboratory of Advanced Welding and Joining, Harbin Institute of Technology, Harbin 150001, China

Abstract: A two-dimensional mathematical model based on volume-of-fluid method is proposed to investigate the heat transfer, fluid flow and keyhole dynamics during electron beam welding (EBW) on 20 mm-thick 2219 aluminum alloy plate. In the model, an adaptive heat source model tracking keyhole depth is employed to simulate the heating process of electron beam. Heat and mass transport of different vortexes induced by surface tension, thermo-capillary force, recoil pressure, hydrostatic pressure and thermal buoyancy is coupled with keyhole evolution. A series of physical phenomena involving keyhole drilling, collapse, reopening, quasi-stability, backfilling and the coupled thermal field are analyzed systematically. The results indicate that the decreased heat flux of beam in depth can decelerate the keyholing velocity of recoil pressure and promote the quasi-steady state. Before and close to this state, the keyhole collapses and complicates the fluid transport of vortexes. Finally, all simulation results are validated against experiments.

Key words: heat transfer; fluid flow; keyhole dynamics; electron beam welding; mass transport; vortex; recoil pressure; backfilling

1 Introduction

When a high-power density electron beam irradiates on the substrate surface, accompanying with strong metal evaporation, a pinhole surrounded by liquid molten metal emerges, which is called as "keyhole". Its existence substantially changes the physical transport mechanism of welding pool, differentiating it from the traditional fusion welding methods [1]. It has been reported that the keyhole, which is not smooth and dynamic fluctuating [2,3], remarkably influences the welding quality and defect formation, such as undercut, humping, porosity, and spiking [4−6].

So far, the extensive research works have been done to study the keyhole dynamics and welding pool's transport phenomena. These works can be summarily divided into two aspects, one based on experimental observation and the other based on numerical calculation. On experimental aspect, X-ray camera, secondary emitted beams, photodiodes and CCD camera technologies have been utilized to observe the formation and fluctuation of keyhole [2,3,7−9]. However, building such observation systems is expensive and time-consuming. Numerical calculation seems a more

promising and desirable tool. On numerical calculation aspect, the VOF or Level Set tracking algorithm, and fluid driving forces combining with ray tracing techniques have been widely adopted to investigate the heat transfer, fluid flow and keyhole dynamics. For example, the formation, backfilling and collapse of keyhole, hydrodynamics of vapor plume, multiple reflections and the coupled heat and mass transports in laser beam welding (LBW) and plasma arc welding (PAW) fields have been researched in depth [10−15]. However, these findings cannot be utilized to reveal the EBW's transport mechanism since their different working pressures [16].

So far, in EBW numerical studies, most of works have mainly concentrated on analyzing the thermal effect and related thermal stress issues [17−19], and thus it is not necessary to trace the detailed keyhole evolution and fluid flow. On the other hand, in order to better predict the weld formation and welding defects, detailed keyhole evolution information is indispensable. However, such kind of researches in EBW field is very limited. RAI et al [16] developed a three-dimensional numerical model to analyze the heat transfer, fluid flow and wall temperature variations on keyhole wall in EBW process at different power density distributions. However, they

ignored the keyhole evolution and its effects on thermal-fluid transport of welding pool. TOMASHCHUK et al [20] utilized a two-dimensional numerical model to simulate the morphology and velocity field distribution in copper–stainless steel dissimilar electron beam welds. However, the keyhole evolution and weld surface deformation are also not considered.

In this work, a 2D mathematical model is proposed to study the thermal-fluid transport phenomena in 2219 aluminum alloy EBW pool. In the model, an adaptive heat source model which can trace the keyhole evolution is employed to simulate the heating process of electron beam. The driving forces of liquid metal in welding pool and heat source model are all implemented by UDF (user-defined function). Based on this model, a series of fluid transport phenomena involving the drilling, collapse, reopening and backfilling of keyhole coupling with heat transfer are analyzed. Finally, all the simulation results are validated against experimental results.

2 Mathematical model

In this work, a 2D computational domain is created (as shown in Fig. 1) and discretized by the finite volume method based on ANSYS Fluent software. And VOF multiphase model is adopted to trace the welding pool's free surface deformation. The whole domain consists of vapor phase, liquid phase (i.e., welding pool), mushy zone and solid phase (i.e., substrate, which is considered as a kind of liquid phase with a very large viscosity). The following assumptions are made in this simulation.

1) Liquid metal of welding pool and gas phase are assumed to be laminar, incompressible and Newtonian fluid.
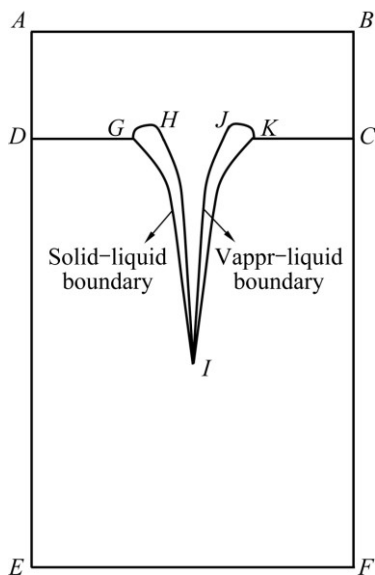

Fig. 1 Schematic sketch of 2D computational domain of EBW process

2) All material properties are temperature-dependent except density.

3) Thermal buoyancy obeys Boussinesq approximation.

4) Plasma formation and multiple reflections inside keyhole are not considered.

2.1 Governing equations

Based on the above assumptions, the conservation equations of mass, momentum and energy are written as

Mass conservation equation:

$$\nabla \cdot \boldsymbol{U} = 0 \tag{1}$$

Momentum equation:

$$\rho\left(\frac{\partial \boldsymbol{U}}{\partial t} + \nabla \cdot (\boldsymbol{UU})\right) = \nabla \cdot (\mu \nabla \boldsymbol{U}) - \nabla p +$$
$$\frac{(1-f)^2}{(f^3+\delta)} A_{\text{mush}} \boldsymbol{U} + P_\sigma + P_r + \rho g \beta (T - T_{\text{ref}}) \tag{2}$$

Energy conservation equation:

$$\frac{\partial}{\partial t}(\rho H) + \nabla \cdot (\rho \boldsymbol{U} H) = \nabla \cdot \left(\frac{k_1}{c_p} \nabla T\right) + q_{\text{ebw}} \tag{3}$$

where $\boldsymbol{U}$ is the velocity vector; p is the pressure, μ is viscosity, ρ is material density, and the third term on the right denotes the momentum sink employed by enthalpy-porosity technique to consider solid−liquid mushy zone, f is the volume fraction of liquid, δ is a relatively small number (0.001) to prevent division by zero; A_{mush} is the mushy zone constant, P_σ is the surface tension acting on liquid−vapor interface which has been transformed by CSF model (continuum surface force) into body force [21], P_r is the evaporation-induced recoil pressure, g is gravity, β is the thermal expansion coefficient, T_{ref} is the reference temperature, H is the enthalpy, c_p is the specific heat capacity, k_1 is the thermal conductivity, and q_{ebw} is the heat flux of electron beam. Specific expressions of surface tension and recoil pressure are as follows:

$$P_r = AB \exp\left(-\frac{\Delta_{\text{vap}} H_m}{RT}\right) \tag{4}$$

$$P_\sigma = \sigma\kappa = \sigma\left(-\nabla \cdot \frac{\boldsymbol{n}}{|\boldsymbol{n}|}\right) \tag{5}$$

where A is a coefficient related to the ambient pressure (0.55 for EBW atmosphere), B is a coefficient related to the material property, $\Delta_{\text{vap}} H_m$ is the latent heat of vaporization, R is mole gas constant, σ is surface tension coefficient, κ is the curvature of free surface, and $\boldsymbol{n}$ is the unit normal vector.

2.2 Tracking of keyhole

In this work, the VOF algorithm is used to track the dynamic profile of keyhole. The function $F(x, y, t)$ is

introduced to describe the fraction of fluid in a computational cell. It satisfies the following governing equation:

$$\frac{\partial F}{\partial t} + \boldsymbol{U} \cdot \nabla F = 0 \tag{6}$$

2.3 Boundary conditions

As shown in Fig. 1, the boundary AB is pressure inlet. AD and BC are pressure outlets. DE, CF and EF are wall boundaries. On vapor−liquid free surface (i.e., keyhole, GHIJK), the material's evaporation and radiation are the only ways of EBW pool's heat dissipation, which can be expressed as

$$k\frac{\partial T}{\partial \boldsymbol{n}} = -q_{rad} - q_{vap} = -\varepsilon k\left(T^4 - T_\infty^4\right) - m_{vap}\Delta_{vap}H_m \tag{7}$$

where ε is the surface radiation coefficient (0.82), k is the Boltzmann constant (5.67×10^{-8}), T_∞ is the ambient temperature (300 K), and m_{vap} is the vaporization rate of material (1.0).

2.4 Heat source model

Figure 2 illustrates the heating mechanism and heat flux distribution of electron beam when the initial electron beam focuses at the superficial base metal. Its kinetic energy is instantaneously transferred into heat energy, which results in melting and evaporation of the material. Accompanying with massive metal vapor, a small keyhole surrounded by the liquid metal emerges. Immediately, the beam deposits its energy into the inner layer beneath the transient keyhole bottom at a depth of δ, which induces new melting and evaporation. In this way, the keyhole is drilled and deepened continuously until the quasi-stable depth is achieved. During this keyholing process, the heat flux of beam at every depth section is decreased gradually due to beam divergence. According to such heating mechanism of electron beam, a heat flux with Gaussian distribution is proposed here with the help of VOF technique. Its specific expressions are as follows:

$$q_{ebw}(x,y,z) = \frac{3\eta Q}{\pi r_0^2 \Delta h(1-e^{-2})}\exp\left[-\frac{3r^2}{r_0^2}\right] \tag{8}$$

$$r_0 = Ah_0^2 + r_f \tag{9}$$

where η is the thermal efficiency, Q is the input power, Δh is the heating depth (0.25 mm), r_0 is the effective beam radius, r_f is the waist radius of beam focused on the upper surface of base metal (0.25 mm), A is an attenuation coefficient (1.25), h_0 is the transient keyhole depth. From Eqs. (8) and (9), it can be seen that the effective beam radius r_0 is increased gradually as the keyholing depth increases, which can better reflect the characteristics of beam divergence.
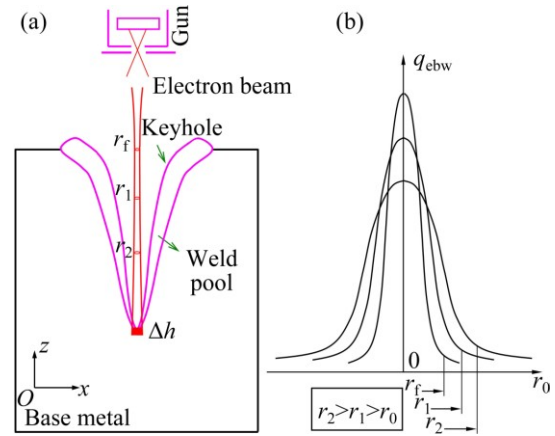

Fig. 2 Schematic diagram of heating mechanism (a) and heat flux distribution (b) of electron beam

2.5 Implementation procedure

In this work, the calculation of heat transfer, fluid flow and keyhole evolution is coupled. The thermo-physical properties of 2219 aluminum alloy and initial values are listed in Table 1. The whole computation domain is divided into an equidistant Cartesian grid by ICEM software, with a total of 40638 cells and 41275 nodes. All related source terms of governing equations and boundary conditions are loaded and compiled by the UDF interface of CFD software FLUENT. Moreover, the spatial discretization of momentum, volume fraction and energy equations adopts the second order upwind scheme. While the discretization of pressure equation adopts the PRESTO

Table 1 Thermo-physical properties of 2219 aluminum alloy and initial values

Property	Value
Density, $\rho/(\text{kg}\cdot\text{m}^{-3})$	2700
Specific heat capacity of solid, $c_s/(\text{J}\cdot\text{kg}^{-1}\cdot\text{K}^{-1})$	871
Specific heat capacity of liquid, $c_l/(\text{J}\cdot\text{kg}^{-1}\cdot\text{K}^{-1})$	1060
Thermal conductivity of solid [13], $k_s/(\text{W}\cdot\text{m}^{-1}\cdot\text{K}^{-1})$	238
Thermal conductivity of liquid [13], $k_l/(\text{W}\cdot\text{m}^{-1}\cdot\text{K}^{-1})$	100
Latent heat of fusion, $H_f/(\text{J}\cdot\text{kg}^{-1})$	3.87×10^5
Latent heat of vaporization, $\Delta_{vap}H_m/(\text{J}\cdot\text{kg}^{-1})$	1.08×10^7
Surface tension at 930 K, $\sigma/(\text{N}\cdot\text{m}^{-1})$	0.914
Thermal coefficient of surface tension, $d\sigma/dT/(\text{N}\cdot\text{m}^{-1}\cdot\text{K}^{-1})$	-0.35×10^{-3}
Solidus line, T_s/K	820
Liquidus line, T_l/K	930
Boiling point in standard conditions, T_b/K	2730
Ambient temperature, T_∞/K	293
Gas constant, $R/(\text{J}\cdot\text{mol}^{-1}\cdot\text{K}^{-1})$	8.31
Acceleration of gravity, $g/(\text{m}\cdot\text{s}^{-2})$	9.81

scheme. Finally, the pressure-implicit with splitting of operators (PISO) algorithm is utilized to solve the whole numerical program.

3 Experimental validation

The experimental material is 20 mm-thick 2219 aluminum alloy plate, welded by KL−110 EBW machine manufactured by Ukraine Paton Welding Institute. Electron beam is focused on the surface of plate with a focus spot of 0.25 mm. Its main technical parameters include accelerating voltage of 60 kV, beam current range of 1−1000 mA, maximum working pressure of 5.332×10^2 Pa, vacuumizing time of 35 min. Figure 3 shows the experimental equipment. In addition, the adopted welding parameters in this simulation are as follows: focus current I_f=730 mA, beam current I_b= 45 mA and heating time t=49 ms. After welding, the weld is cut, polished, etched and inlaid.
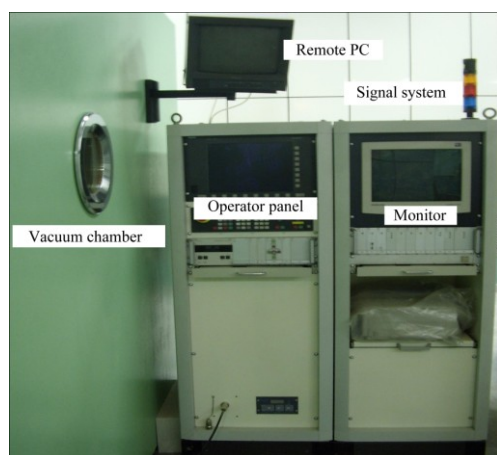

Fig. 3 Photograph of KL−110 EBW machine

In order to validate the proposed numerical model, the following cases are utilized. Firstly, Fig. 4 compares the results of calculated and experimental weld shapes. From Fig. 4, it can be seen that the calculated and experimental weld shapes agree well with each other. Because the weld shape is the comprehensive effect of heat transfer, fluid flow and keyhole deformation, this

comparison result indirectly proves the correctness and reasonability of the mathematical model. Secondly, Fig. 5 illustrates the microstructure distribution in depth direction of weld. It can be observed that the grain sizes of microstructure are decreased gradually from the top to the bottom, which further validates the correctness of the simulated cooling rate. Finally, more detailed weld dimension comparisons including the weld width, penetration and depth of arc crater are shown in Table 2. From Table 2, it can be seen that their errors are all within 10%. From the above analysis, it can be seen that the correct and reasonable numerical results can be obtained by utilizing the proposed 2D mathematical model.
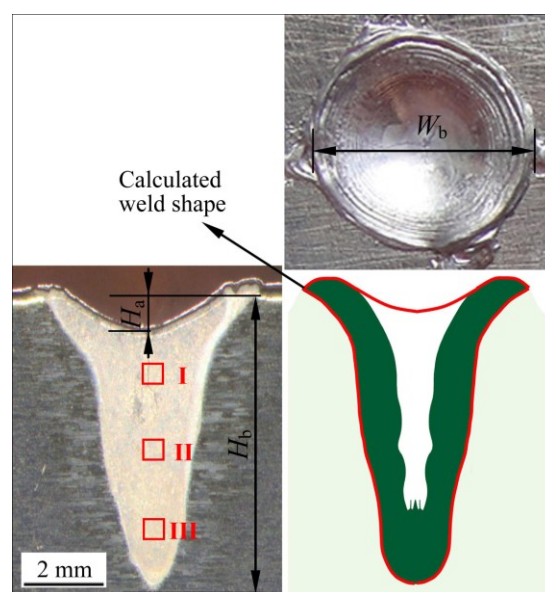

Fig. 4 Comparison of calculated and experimental weld shape

Table 2 Weld shape dimension comparisons

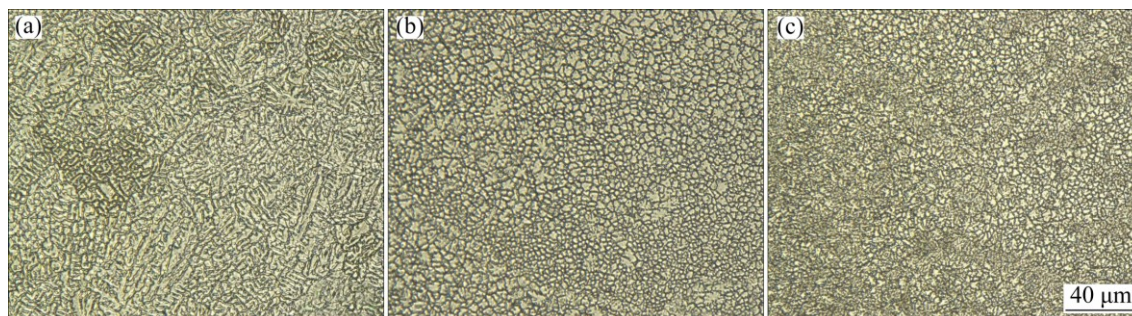| Item	Weld width, W_b/mm	Penetration, H_b/mm	Depth of arc crater, H_a/mm
Experimental value	5.65	7.35	1.26
Calculated value	5.75	7.23	1.21
Error/%	1.77	1.63	3.97

Fig. 5 Microstructure distribution in depth direction of weld: (a) Zone I in Fig. 4; (b) Zone II in Fig. 4; (c) Zone III in Fig. 4

4 Results and discussion

4.1 Temperature field of EBW pool

Figure 6 shows the temperature distribution of 2219 aluminum alloy EBW pool at different time during the heating stage. Different colors in Fig. 6 represent the magnitude of temperature. Firstly, at the initial time t= 1.0 ms (see Fig. 6(a)), the electron beam bombards the surface layer of substrate, and promotes the formation of a small welding pool. Because its peak temperature is lower than boiling point of the material, no vaporization happens. As time goes on, the peak temperature of welding pool rises rapidly to 2300 K at t=3.0 ms (Fig. 6(b)). Meanwhile, at this moment, the maximum recoil pressure at the keyhole bottom reaches about 1×10^4 Pa, which corresponds to the current material's boiling point of 2300 K. High-temperature liquid metal of welding pool begins to vaporize. Under the action of metal vapor, the pool concaves and forms a pinhole, i.e., keyhole. Immediately, the beam in real-time follows and focuses on the bottom of keyhole. By this way, the pool

is elongated continuously, resulting in an increased penetration (Fig. 6(c)). In addition, from Fig. 6(c), it can also be found that most of welding pool adjacent to the keyhole sidewall has a low temperature (930−1200 K). This is mainly because, in EBW pool, the liquid metal is short of energy supply by the direct radiation of beam. When t=40 ms, the middle−upper part of keyhole collapses inward to form a meeting-point (Fig. 6(d)), which prevents the beam from further heating the keyhole bottom and thus resulting in the decreasing liquid metal's temperature beneath it. Meanwhile, the beam promptly vaporizes the meeting-point and reopens the keyhole at t=43 ms (Fig. 6(e)). So, it can be found that the peak temperature emerges at the keyhole bottom again. At last, the welding pool reaches its quasi-steady depth at t=49 ms, where the beam energy balances with heat conduction, radiation and vaporization (Fig. 6(f)).

Figure 7 shows the temperature evolution during the cooling stage of welding pool. With the disappearance of beam energy and evaporation process, the temperature declines sharply and is lower than pool's boiling point at t=52 ms. In addition, it can be also found that the depth
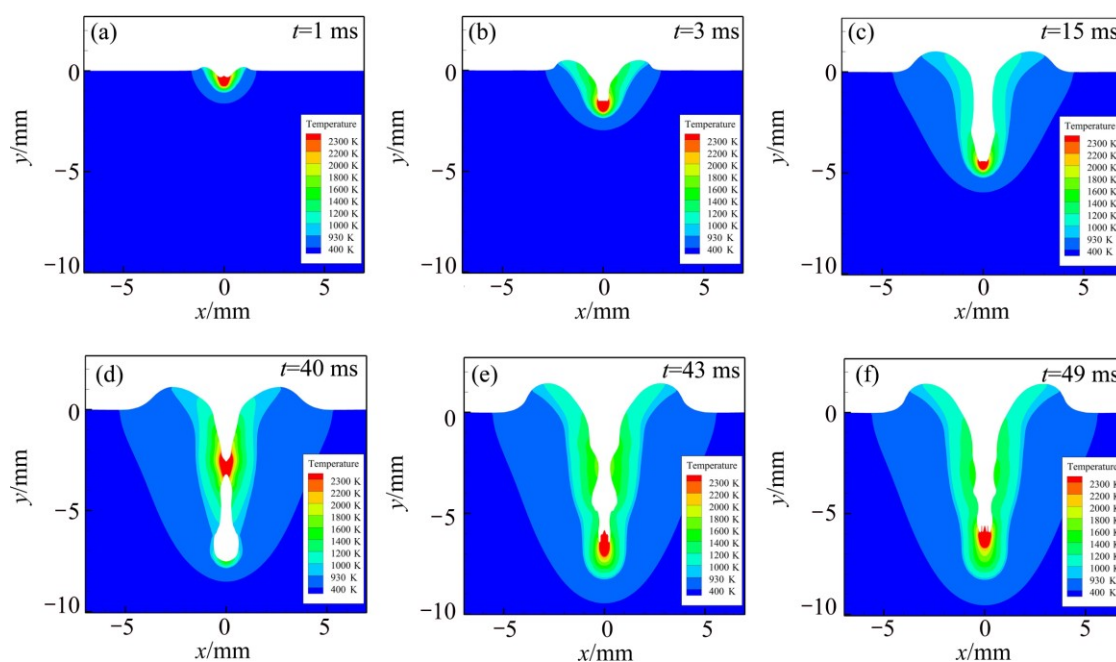

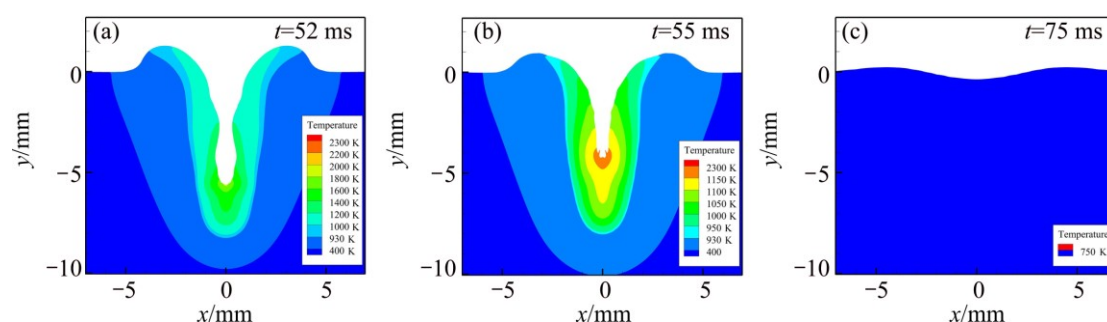**Fig. 6** Computed temperature fields during heating stage

Fig. 7 Computed temperature fields during cooling stage

of keyhole decreases rapidly as the backfilling process of liquid metal continues. During this process, the pool's temperature declines continuously (Fig. 7(b))and is lower than the solidus line at 75 ms (Fig. 7(c)).

4.2 Fluid field of EBW pool and keyhole evolution

Figure 8 shows the fluid flow behavior of welding pool with a keyhole evolution during heating stage of EBW process. The velocity vector and magnitude as well as flow patterns are labeled in its sub-figures. At the initial time t=1 ms (Fig. 8(a)), the superficial metal of substrate firstly melts and forms a small welding pool. Because the heating duration of beam is very short, no vaporization occurs. Thus, the thermal-fluid driving forces are merely surface tension, thermo-capillary force and hydrostatic pressure. Under their influences, the liquid metal at the centre of pool firstly flows to its edge, and then flows downward and returns to the pool's bottom centre, forming a pair of symmetrical vortexes. According to flow direction, each vortex is divided into two sub-vortexes "1" and "2". The sub-vortex 1 mainly helps transport the liquid metal from the bottom of keyhole upward to its opening region, resulting in an extended weld width. The sub-vortex 2 mainly helps to transport the liquid metal downward along solid−liquid boundary to backfill the keyhole. As time goes on, when t=3 ms, the evaporation process occurs in the interaction zone between beam and welding pool (Fig. 8(b)). The resulting recoil pressure depresses the vapor−liquid free surface of pool and an obvious keyhole forms. At this moment, it can be found clearly that the magnitude of sub-vortex 1 (maximum flow velocity v_{max}≈2.53 m/s) increases significantly and is larger than that of

sub-vortex 2. In this way, the penetration and width of welding pool increase gradually by the continuous keyhole-drilling of recoil pressure and transportation of vortexes (Fig. 8(c)). Moreover, the former increases remarkably, while the latter increases slightly. As keyholing process continues, the keyhole instability and the accumulated amount of liquid metal adjacent to keyhole wall are increased gradually. When the accumulated amount exceeds a certain value, the keyhole collapses and converges at the middle−upper meeting-point (Fig. 8(d)). Above the meeting-point, the previous vortexes continue to play their roles. While within the region beneath the meeting-point, the sub-vortexes 3 (v_{max}≈1.10−2.05 m/s) and 4 (v_{max}≈0.56−0.75 m/s) emerge due to the collapse of keyhole. The former notably transports liquid metal downward to backfill the cooling keyhole bottom. The latter slightly transports liquid metal upward. Subsequently, under the influence of recoil pressure induced by the refocused beam on the meeting-point, the collapsed keyhole is reopened again (Fig. 8(e)). Furthermore, from Fig. 8(e), it can be further found that the sub-vortexes 5 and 6 emerge at the bottom of keyhole besides the previous vortexes. This marks that the beam energy is insufficient at this depth, so the pool cannot be obviously drilled. Finally, when t=49 ms, all driving forces achieve a quasi-steady balance and thus the welding penetration no longer continues to increase, as shown in Fig. 8(f). Throughout Fig. 8, it is noted that the keyhole fluctuates all the time. This phenomenon agrees with some previous experimental results [2,3].

Figure 9 shows the fluid flow behavior of welding pool during the backfilling stage of keyhole at the cooling stage. At the initial cooling time t=52 ms
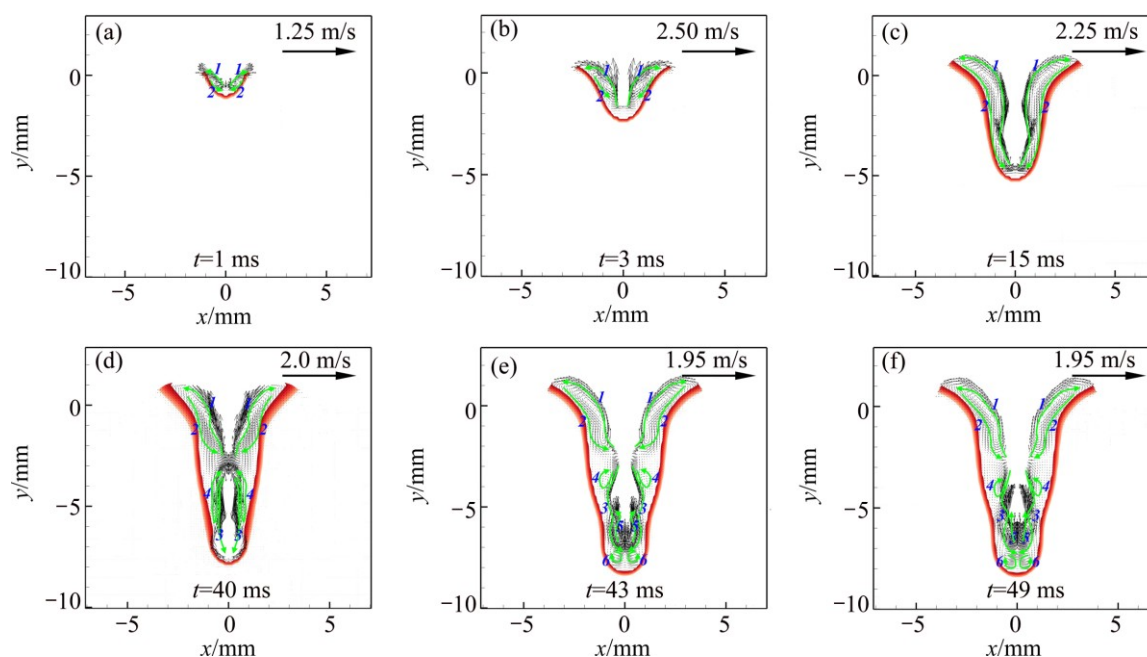

Fig. 8 Computed flow fields with different flow patterns during heating stage
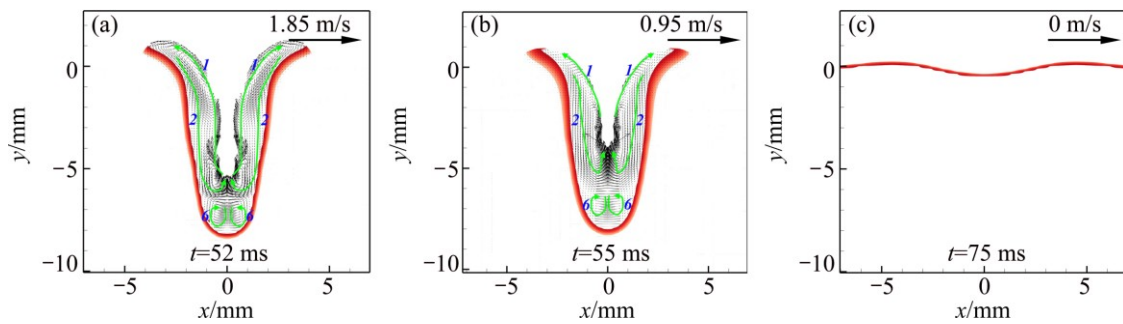
Fig. 9 Computed flow fields with different flow patterns during cooling stage

(Fig. 9(a)), with the disappearance of recoil pressure, the keyhole is rapidly backfilled under the influence of sub-vortex 2 ($v_{max} \approx 1.85$ m/s). Contrary to the flow state in Fig. 8, at this moment, the magnitude of sub-vortex 2 is greater than that of sub-vortex 1. In addition, the previous sub-vortex 6 still exists at the bottom of pool. In this way, the keyhole is continuously backfilled (Fig. 9(b)) until the whole welding pool completely is solidified at $t=75$ ms (Fig. 9(c)).

Figure 10 illustrates the relationship between the evolution of keyhole depth and time. From the curve, it can be seen that the keyhole-drilling speed of recoil pressure decreases gradually with increasing the keyhole depth during heating stage. This is mainly due to the attenuation characteristic of beam energy along plate thickness direction (Eqs. (8) and (9)). But during the cooling stage, the keyhole depth decreases sharply due to the strong backfilling transportation of sub-vortex 2. Moreover, from Fig. 10, it can be seen that the average backfilling speed of welding pool is obviously higher than its drilling speed.
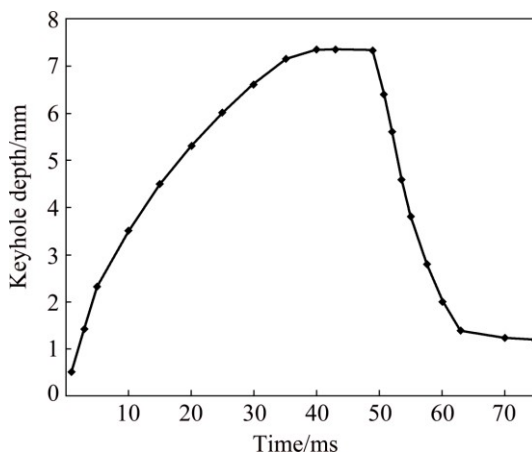

Fig. 10 Keyhole depth evolution during whole thermal cycle stages

5 Conclusions

1) A 2D numerical model has been proposed to investigate the coupled transport behavior of thermal-fluid during electron beam welding of 20 mm-thick 2219 aluminum alloy and validated against experiment.

2) The agreement between the calculation results and the corresponding experimental results indicates that the proposed 2D numerical model is feasible and reliable for a description of physical phenomena during EBW process.

3) The decreased heat flux of electron beam well simulated by the adaptive heat source model results in the gradual deceleration of keyholing velocity of recoil pressure and promotes the emergence of quasi-stable state.

4) As the keyholing depth increases, the keyhole instability is increased gradually. Before reaching the quasi-stable state, the keyhole collapses and results in a more complicated fluid transport of vortexes. In addition, the keyhole collapse implies that the beam energy is insufficient to further drill the molten pool.

References

[1]   LACKI P, ADAMUS K. Numerical simulation of the electron beam welding process [J]. Computers and Structures, 2011, 89: 977−985.

[2]   ARATA Y, ABE E, ODA T. Fundamental phenomena in high power CO_2 laser welding [J]. Transactions of JWRI, 1985, 14: 5−22.

[3]   PETROV P, GEORGIEV C, PETROV G. Experimental investigation of weld pool formation in electron beam welding [J]. Vacuum, 1998, 51(3): 339−343.

[4]   WEI P S, CHAO T C. Prediction of pore size in high power density beam welding [J]. International Journal of Heat & Mass Transfer, 2014, 79: 223−232.

[5]   CHI C T, CHAO C G, LIU T F, WANG C C. Optimal parameters for low and high voltage electron beam welding of AZ series magnesium alloys and mechanism of weld shape and pore formation [J]. Science and Technology of Welding & Joining, 2008, 13(2): 199−211.

[6]   KAI Li, LU Feng-gui, GUO Song-tao, CUI Hai-chao, TANG Xin-hua. Porosity sensitivity of A356 Al alloy during fiber laser welding [J]. Transactions of Nonferrous Metals Society of China, 2015, 25: 2516−2523.

[7]   LIU Zu-ming, WU Chuan-song, GAO Jin-qiang. Vision-based observation of keyhole geometry in plasma arc welding [J]. International Journal of Thermal Sciences, 2013, 63: 38−45.

[8]   LUO M, SHIN Y C. Vision-based weld pool boundary extraction and width measurement during keyhole fiber laser welding [J]. Optics & Lasers in Engineering, 2015, 64: 59−70.

[9] GAO Jin-qiang, QIN Guo-liang, YANG Jia-lin, HE Jian-guo, ZHANG Tao, WU Chuan-song. Image processing of weld pool and keyhole in Nd:YAG laser welding of stainless steel based on visual sensing [J]. Transactions of Nonferrous Metals Society of China, 2011, 21: 423−428.

[10] CHO W I, Na S J, THOMY C, VOLLERTSEN F. Numerical simulation of molten pool dynamics in high power disk laser welding [J]. Journal of Materials Processing Technology, 2012, 212: 262−275.

[11] CHO J H, FARSON D F, MILEWSKI J O, HOLLIS K J. Weld pool flows during initial stages of keyhole formation in laser welding [J]. Journal of Physics D: Applied Physics, 2009, 42: 175502.

[12] TAN W, BAILEY N S, SHIN Y C. Investigation of keyhole plume and molten pool based on a three-dimensional dynamic model with sharp interface formulation [J]. Journal of Physics D: Applied Physics, 2013, 46: 055501.

[13] ZHANG Yi-ming, SHEN Zhong-hua, NI Xiao-wu. Modeling and simulation on long pulse laser drilling processing [J]. International Journal of Heat & Mass Transfer, 2014, 73: 429−437.

[14] FAN H G, KOVACEVIC R. Keyhole formation and collapse in plasma arc welding [J]. Journal of Physics D: Applied Physics, 1999, 32: 2902−2909.

[15] WU C S, ZHANG T, FENG Y H. Numerical analysis of the heat and fluid flow in a weld pool with a dynamic keyhole [J]. International Journal of Heat and Fluid Flow, 2013, 40: 186−197.

[16] RAI R, BURGARDT P, MILEWSKI J O, LIENERT T J, DEBROY T. Heat transfer and fluid flow during electron beam welding of 21Cr−6Ni−9Mn steel and Ti−6Al−4V alloy [J]. Journal of Physics D: Applied Physics, 2009, 42: 025503.

[17] LUO Yi, YOU Guo-qiang, YE Hong, LIU Jin-he. Simulation on welding thermal effect of AZ61 magnesium alloy based on three-dimensional modeling of vacuum electron beam welding heat source [J]. Vacuum, 2010, 84: 890−895.

[18] FERRO P, ZAMBON A, BONOLLO F. Investigation of electron-beam welding in wrought Inconel 706−Experimental and numerical analysis [J]. Materials Science and Engineering A, 2005, 392: 94−105.

[19] SMITH D J, ZHENG G, HURRELL P R, GILL C M, PELLEREAU B M E, AYRES K, GOUDAR D, KINGSTON E. Measured and predicted residual stresses in thick section electron beam welded steels [J]. International Journal of Pressure Vessels and Piping, 2014, 120−121: 66−79.

[20] TOMASHCHUK I, SALLAMAND P, JOUVARD J M, GREVEY D. The simulation of morphology of dissimilar copper–steel electron beam welds using level set method [J]. Computational Materials Science, 2010, 48: 827−836.

[21] BRACKBILL J U, KOTHE D B, ZEMACH C. A continuum method for modeling surface tension [J]. Journal of Computational Physics, 1992, 100: 335−354.

2219 铝合金板电子束焊接过程热流传输行为的数值分析

刘成财，何景山

哈尔滨工业大学 先进焊接与连接国家重点实验室，哈尔滨 150001

摘 要： 提出一种基于有限体积法的二维数学模型，以研究 20 mm 厚 2219 铝合金板在电子束焊接过程的热传递、流体流动以及匙孔的动力学行为。采用一种能够实时跟踪匙孔深度的自适应热源模型来数值模拟电子束的加热过程。由表面张力、热毛细力、反冲压力、流体静压力以及热浮力等诱导的不同涡旋的热和质量输运作用与匙孔演变相互耦合。详细分析了一系列物理现象，包括电子束焊接过程中的匙孔钻取、塌陷、重新打开、准稳态过程、回填过程以及在此过程中的温度变化。结果表明，深度方向降低的电子束热流能减慢反冲压力的匙孔钻取速度，并促进准稳定状态的出现。在准稳定状态出现之前，匙孔会发生塌陷并加剧涡旋流体输运的复杂性。最后，所有的计算结果与实验结果进行对比，来验证数学模型的可行性。

关键词： 热传递；流体流动；匙孔动力学；电子束焊接；质量传输；涡旋；反冲压力；回填

(Edited by Wei-ping CHEN)